


Article

Monte Carlo Simulation of Quantum-Cutting Nanocrystals as the Luminophore in Luminescent Solar Concentrators

Qi Nie [†] , Wenqing Li [†] and Xiao Luo ^{*†} 

School of Optoelectronic Science and Engineering, University of Electronic Science and Technology of China (UESTC), Chengdu 610054, China; 202222050632@std.uestc.edu.cn (Q.N.); 202322050737@std.uestc.edu.cn (W.L.)

* Correspondence: luox@uestc.edu.cn

[†] These authors contributed equally to this work.

Abstract: Quantum-cutting luminescent solar concentrators (QC-LSCs) have great potential to serve as large-area solar windows. These QC nanocrystals can realize a photoluminescence quantum yield (PLQY) of as high as 200% with virtually zero self-absorption loss. Based on our previous work, we have constructed a Monte Carlo simulation model that is suitable to simulate the performance of the QC-LSCs, which can take into account the band-edge emissions and near-infrared emissions of the QC-materials. Under ideal PLQY conditions, CsPbCl_xBr_{3-x}:Yb³⁺-based LSCs can reach 12% of the size-independent external quantum efficiency (η_{ext}). Even if LSCs have a certain scattering factor, the CsPbCl_xBr_{3-x}:Yb³⁺-based LSCs can still obtain an η_{ext} exceeding 6% in the window size (>1 m²). The flux gain (FG) of the CsPbCl_xBr_{3-x}:Yb³⁺-based LSC-PV system can reach 14 in the window size, which is a very encouraging result.

Keywords: nanocrystals; luminescent solar concentrators; quantum cutting; Monte Carlo simulation; quantum efficiency



Citation: Nie, Q.; Li, W.; Luo, X. Monte Carlo Simulation of Quantum-Cutting Nanocrystals as the Luminophore in Luminescent Solar Concentrators. *Photonics* **2024**, *11*, 553. <https://doi.org/10.3390/photonics11060553>

Received: 9 May 2024

Revised: 27 May 2024

Accepted: 5 June 2024

Published: 12 June 2024



Copyright: © 2024 by the authors. Licensee MDPI, Basel, Switzerland. This article is an open access article distributed under the terms and conditions of the Creative Commons Attribution (CC BY) license (<https://creativecommons.org/licenses/by/4.0/>).

1. Introduction

Building-integrated photovoltaic (BIPV) is proposed to help near-zero-energy buildings to reduce their carbon emissions. BIPV, which aims to integrate photovoltaic elements into the building envelope, can replace the conventional materials of roofs, walls and windows [1,2]. Very recently, luminescent solar concentrators (LSCs) have been widely researched, which are quite suitable for constructing solar windows [3–5]. The LSC-PV windows' surfaces are free of electrodes and can be selected due to their color and transparency, thus better meeting the aesthetic and practical needs of buildings. LSCs are sunlight collectors that absorb incident solar photons, emit photoluminescence photons, and waveguide these photons via total internal reflection to the edges [6]. Therefore, the LSCs do not need additional solar tracking systems, which are expensive. Common luminophores for LSCs often suffer from reabsorption loss and nonradiative recombination. To address this issue, recent work has reported luminophore materials with low reabsorption as well as high photoluminescence quantum efficiency (PLQY). For example, Li et al. reported that they synthesized a 4,4'-(benzo[c][1,2,5] thiadiazole-4,7-diyl) bis (N,N-diphenylaniline) AIE-emitter, which displayed a near-unity emission quantum yield in a matrix with a large Stoke shift of 0.59 eV [7]. Additionally, they engineered the surface texture of the PDMS matrix by using a bioinspired nanolithography method with a natural lotus leaf as the template to build LSCs that inherited the superhydrophobic, self-cleaning properties. Gungor et al. synthesized Zn-doped CuInSe_{2-x}S_x/CuInS₂ quantum dots with a Stoke shift of 0.15 eV and PLQY of 78% and used this quantum dots to build the LSCs with an external quantum efficiency of 11.7% and dimensions of 9.5 cm × 9.5 cm × 0.77 cm [8]. Park et al. introduced a new, laminated type of LSC structure, where a patterned low-refractive-index medium acts as an optical 'guard rail', providing a practically non-decaying path to guide photons. They

found that the external quantum efficiencies at 450 nm are 45% for a 100 cm² area [3]. Very recently, Wang et al. fabricated large-area (~100 cm²) tandem LSCs based on highly stable carbon dots and highly luminescent near-infrared emitting CuInSe_{2-x}S_x/ZnS QDs [9]. The PL emitters have large Stoke shifts and high PL QYs, of 54% for UV-active CDs and 61% for NIR-emitting CuInSe_{2-x}S_x/ZnS QDs. Wang et al. synthesized high-quality lead-free Cs₃Cu₂Cl₅ perovskite nano-disks with a high photoluminescence quantum yield of 84.2% and a large Stokes shift of 1.43 eV [10]. LSC luminophores, such as organic dyes [11,12], colloidal quantum dots [8,13–17], and carbon dots [18–21], have rapidly developed in recent years. However, the PLQY of most of these materials is typically less than 100%, and thus the internal quantum efficiency (η_{int}) of the LSC is limited to 75%.

Recently, various excellent dopant examples have been demonstrated, including the main group elements [22,23], transition metals [17,24], and rare earth elements [25–27]. Rare earth Yb³⁺ ion is not only an important doping candidate for fundamental studies of doping chemistry but also has high application potential. For example, Milstein et al. first described the hot injection synthesis of Yb³⁺:CsPbCl₃ nanocrystals with analytical Yb³⁺ concentrations of as high as 7.5% and replicable PLQYs exceeding 100% [28]. They believed that energy captured by a Yb³⁺-induced defect can subsequently be transferred to two neighboring Yb³⁺ ions in a single concerted step at the picosecond time scale. Ding et al. demonstrated Cr³⁺, Yb³⁺, and Ce³⁺ tri-doped CsPbCl₃ perovskite quantum dots and they integrated them with silicon photodetectors [25]. These quantum dots have a total PLQY of 188% and excellent stability due to the Ce³⁺ doping. The response of silicon photodetectors successfully expanded to the deep UV region, realizing the full spectrum response within 200–1100 nm. Cai et al. reported that they synthesized Mn²⁺/Yb³⁺ co-doped CsPbCl₃ nanocrystals, which showed unique triple-wavelength emissions covering the ultraviolet/blue, visible, and near-infrared regions [24], and achieved a total PLQY of 125.3%. Gao et al. achieved efficient Yb³⁺ infrared emissions from both quantum cutting and up-conversion, demonstrated by adjusting Er³⁺ and Yb³⁺ concentrations [27]. Shen et al. synthesized Yb³⁺-doped CsPbCl_xBr_{3-x} perovskite nanocrystals to build electroactivated NIR LEDs [29]. Xu et al. directly identified the doped Yb³⁺ in CsPbCl₃ perovskites using state-of-the-art transmission electron microscopy and three-dimensional atom probe tomography at the atomic scale [30]. They proved that Yb³⁺ simultaneously replaces Pb²⁺ and occupies the lattice interstitial sites. This work provides an atomic-level understanding of the doping mechanism in perovskites.

Based on our previous work [31], we first introduce the quantum cutting (QC) materials into the LSCs. Yb³⁺-doped CsPbCl₃ nanocrystal (NC) with an ultrahigh PLQY of 164% and 25 cm² QC-LSC with an η_{int} of 118.1% are presented in our previous work. In the QC progress, the formation of shallow Yb³⁺-induced defects play a crucial role in facilitating a picosecond, nonradiative, energy-transfer process. This progress can de-excite the photoexcited perovskite nanocrystal and simultaneously excite two Yb³⁺ dopant ions [28,32,33]. The luminescence of Yb³⁺ is ~990 nm, located at the high-EQE region of silicon-based PV cells [34]. Very recently, many new solar cells have emerged, such as organic PV cells, perovskite PV cells, and GaAs PV cells, which may be suitable for LSCs [35–37], but we should consider both their cost and efficiency. Some of these PV cells suffer from low power conversion efficiency, such as organic PV cells and perovskite PV cells, while others suffer from a high price, such as GaAs PV cells. Therefore, silicon-based PV cells are the best candidate for commercialized LSCs.

The schematic principle of the QC-LSC-PV system is shown in Figure 1. The system is simply composed of QC luminophores, a waveguide medium, and silicon-based PV cells. The red arrows represent the QC emission progress and the blue arrows represent the band-edge emission progress. When the sunlight is incident on the face of the LSC, some of the photons are absorbed by the luminophores and new photons are emitted according to their emission spectra; the remaining photons that are not absorbed transmit from the bottom surface. As for the QC-LSC, most of the incident photons will undergo the QC process and emit ~990 nm NIR fluorescence and some of them will go through band-edge

emission or loss through nonradiative recombination. Some of the emitted photons in the waveguide medium will enter the escape cone or enter the total internal reflection mode. The band-edge emitted photons may be reabsorbed and re-emit new photons depending on the PLQY of the luminophore. In the end, some of the emitted photons will reach the LSC's edges and be absorbed by the coupled silicon-based solar cells to produce energy.

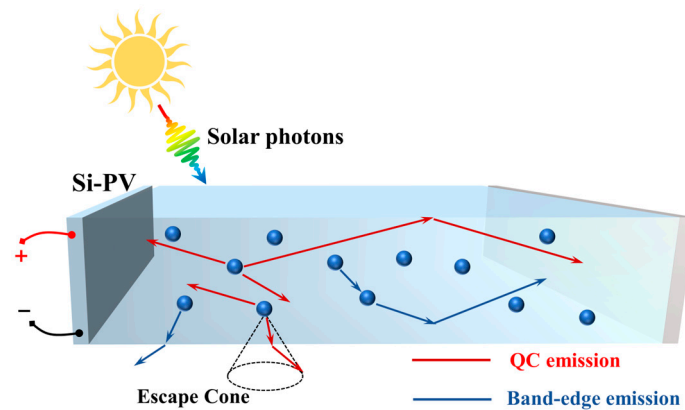


Figure 1. A schematic representation of QC-based LSC-PV systems.

In this work, we present a Monte Carlo simulation model for evaluating the performance of QC-LSCs. The model considers both the band-edge intrinsic emissions and near-infrared QC emissions of fluorescent materials. Additionally, the as-synthesized $\text{CsPbCl}_3:\text{Yb}^{3+}$ and $\text{CsPbCl}_x\text{Br}_{3-x}:\text{Yb}^{3+}$ nanocrystals have negligible reabsorption and a weak band-edge emission. The spectral data of the two materials were input into our MC simulation model to predict the performance of the QC-LSCs. The simulation results demonstrate the competition between band-edge luminescence and Yb^{3+} ion luminescence. In an ideal situation, $\text{CsPbCl}_x\text{Br}_{3-x}:\text{Yb}^{3+}$ -based LSC can reach external quantum efficiency (η_{ext}) of 12.3% and there is the potential to apply the $\text{CsPbCl}_x\text{Br}_{3-x}:\text{Yb}^{3+}$ -based LSC to large-area devices. We also discussed the QC-LSC-PV system and found that the $\text{CsPbCl}_x\text{Br}_{3-x}:\text{Yb}^{3+}$ -based LSC-PV system can reach a flux gain (FG) of as high as 14 when the LSC area exceeds 1 m^2 .

2. Monte Carlo Simulation

Monte Carlo (MC) simulation is a very effective way to explore the performance characteristics of LSCs, as the principle of LSCs does not involve phase-dependent wave effects such as interference and diffraction. MC simulation is actually a representation of a statistical law. When enough events are simulated, it will exhibit physical laws close to the actual situation. When all the practical considerations of LSCs are involved, the simulation results will match the actual situation. In this work, we built an MC simulation model which is suitable for quantum-cutting the luminophore of LSC. Figure 2 illustrates the logic block diagram of the MC simulation.

In order to emulate the solar spectrum, each randomly generated photon will carry information about its wavelength and coordinates. When the number of randomly generated photons reaches about one million to one hundred million, the statistical distribution of photons for different wavelengths will be highly similar to the solar spectrum. By considering the solar spectrum as a probability density function and transforming it into a cumulative distribution function, we can obtain information about the wavelength of each randomly generated photon. In this work, all the sunlight energy is considered to be uniformly incident on the surface of the LSC. To obtain coordinates of the random photons, we grid the surface of LSC, and the length of each grid is L/N , where L represents the length of the LSC and N represents the number of randomly generated photons. The coordinates of all photons are randomly distributed to grid points on the surface.

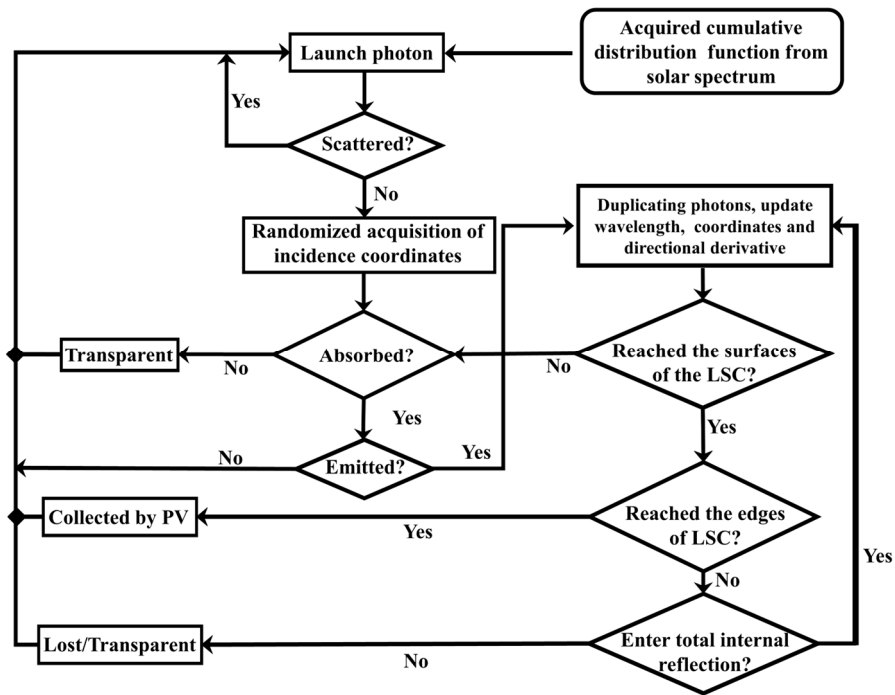


Figure 2. Schematic representation of the Monte Carlo algorithm.

When each photon is randomly generated, it undergoes scattering, absorption, re-emission, re-absorption, and total reflection. The surface scattering can be calculated as follows:

$$R = \left(\frac{n_1 - n_0}{n_1 + n_0} \right)^2 = \left(\frac{1.5 - 1}{1.5 + 1} \right)^2 = 0.04, \tag{1}$$

where n_1 is the refractive index of LSC waveguide and n_0 is the refractive index of air. Absorbance can be determined using the Lambert–Beer Law and the possible distance, ΔS , travelled by each photon in the LSC waveguide medium can also be obtained by the Lambert–Beer Law:

$$\Delta S = -\frac{l \times \log_{10}(1 - \delta)}{OD}, \tag{2}$$

where OD is the optical density of each material and l is the length of the cuvette. δ denotes a random number range of $[0, 1]$. If scattering coefficient, s , is not ignored, Equation (2) can be rewritten as follows:

$$\Delta S = -\frac{\log_{10}(1 - \delta)}{OD/l + s/\ln 10} \tag{3}$$

The scattering coefficient is defined using the Lambert–Beer Law using exponent e , and Equation (2) is defined using the Lambert–Beer Law using exponent 10. Therefore, it is necessary to transform the value of s into a calculation under the condition that the exponent is 10. When a photon has travelled ΔS , some of the photons are considered to be absorbed, while the rest are scattered, i.e., the direction of motion of the photons is updated. If a photon is absorbed, it is re-emitted according to the PLQY.

$$\xi < \eta_{PL}, \tag{4}$$

where ξ is another random number that refers to quantum yield range of $[0, 1]$. Considering that the QC luminophore has NIR emissions and band-edge emissions, we redefine the inequality (4). We suppose that the PLQY of band-edge emissions is α and the PLQY of NIR emissions is β . When the ξ is smaller than the α , the emit-photon will change its wavelength information according to the band-edge emission spectrum. When the ξ is larger than the α and smaller than $\alpha + \beta/2$, the emitting photon will change its wavelength information

according to the NIR emission spectrum and the NIR emissions photon will be duplicated. If ξ is larger than $\alpha + \beta/2$, we will consider that nonradiative recombination will occur.

When the photon is re-emitted or scattered, the photon's position and directional derivatives will be updated. Because the materials are isotropic, the updated photon coordinate is as follows:

$$\begin{aligned}x_{new} &= x_{old} + u_x \Delta S \\y_{new} &= y_{old} + u_y \Delta S \\z_{new} &= z_{old} + u_z \Delta S\end{aligned}\quad (5)$$

where $(x_{old}, y_{old}, z_{old})$ are the photon's old coordinates, $(x_{new}, y_{new}, z_{new})$ are the photon's new coordinates, and (u_x, u_y, u_z) are the photon's direction cosines. u_x , u_y and u_z can expressed as follows:

$$\begin{aligned}u_x &= \sin \theta \cos \phi \\u_y &= \sin \theta \sin \phi \\u_z &= \cos \theta\end{aligned}\quad (6)$$

where θ is the zenith angle, which is obtained by $\cos \theta = 2a - 1$, $a \in [0, 1]$, and ϕ is the azimuthal angle, which is obtained by $\phi = 2\pi b$, $b \in [0, 1]$. Therefore, the re-emitted and scattered light is isotropically distributed.

When the photon reaches the surfaces of the LSC, whether the photon enters the internal total reflection or exits from the top or bottom surface will be determined. The η_{int} is defined as the ratio of the number of photons reaching the edges to the number of photons emitted by the luminophores and the η_{ext} is defined as the ratio of the number of photons reaching the edges to the number of solar photons. In this work, we consider the coupling of the PV cells to the LSC's edges to be perfect. When photons reach the edges, they are considered to be absorbed by the edge-coupled PV cells, and then the determination of the next photon is carried out. In this work, we used a full polymer LSC with a thickness of $d = 0.5$ cm as the model for the analysis. The length (L) of the LSCs varies from 5 cm to 150 cm.

3. Experiments

Materials. 1—Octadecene (ODE, technical grade, 90%) and oleic acid (OA, technical grade, 90%) were purchased from Sigma Aldrich, Beijing, China. Oleyl amine (OAm, 80–90%) and ethyl acetate (EtOAc, AR 99%), were purchased from Macklin, Shanghai, China, lead acetate trihydrate ($\text{Pb}(\text{OAc})_2 \cdot 3\text{H}_2\text{O}$, 99.998%), cesium acetate (CsOAc , 99.99%), trimethylsilyl chloride (TMS-Cl, 98%), trimethylsilyl bromo (TMS-Br, 98%), and hexanes (AR, 97%) were purchased from Aladdin, Shanghai, China. Ytterbium acetate hydrate ($\text{Yb}(\text{OAc})_3 \cdot 4\text{H}_2\text{O}$, 99.9%) was purchased from Sigma Aldrich. Anhydrous ethanol (ACS; HPLC Certified 99.9%) was purchased from J&K, Beijing, China. All chemicals were used as received without further purification.

$\text{CsPbCl}_3:\text{Yb}^{3+}$ Nanocrystal (NC) synthesis. $\text{CsPbCl}_3:\text{Yb}^{3+}$ NCs were synthesized by hot injection following the procedures. Briefly, 5.0 mL ODE, 0.5 mL OAm, 1.0 mL OA, 0.2 mmol $\text{Pb}(\text{OAc})_2 \cdot 3\text{H}_2\text{O}$, 0.28 mL of 1 M CsOAc in ethanol, and 0.16 mmol $\text{Yb}(\text{OAc})_3 \cdot 4\text{H}_2\text{O}$ were added to a 50 mL round-bottom flask. This solution was stirred and degassed at room temperature for 5 min before heating to 120 °C, and the solution was then degassed for 1 h. The reaction vessel was then flushed with N_2 and heated to 240 °C. Upon reaching this temperature, 0.2 mL of TMS-Cl in 0.5 mL ODE was swiftly injected. Immediately after injection, the flask was cooled to room temperature using a water bath. The NCs were separated from the crude solution by centrifuging at 3350 rpm. After being dispersed in hexane, the NCs were washed again with EtOAc.

$\text{CsPbCl}_x\text{Br}_{3-x}:\text{Yb}^{3+}$ Nanocrystal synthesis. The $\text{CsPbCl}_3:\text{Yb}^{3+}$ NCs were dissolved by hexane the solution was placed in a 1 cm path length cuvette under N_2 . A certain amount of 0.1 M TMS-Br solution was added to the cuvette. The next day, we could obtain the target product of $\text{CsPbCl}_x\text{Br}_{3-x}:\text{Yb}^{3+}$ NCs. The solvent was evaporated and the target product was redissolved in hexane for further use.

4. Results and Discussion

We synthesized $\text{CsPbCl}_3:\text{Yb}^{3+}$ nanocrystal. Figure 3a shows a transmission electron microscopy (TEM) image of $\text{CsPbCl}_3:\text{Yb}^{3+}$ NCs with average edge lengths of ~ 15 nm. The absorption spectrum of the nanocrystal is shown in the blue curve of Figure 3b, with the onset of absorption occurring at approximately 410 nm. The emission spectrum is shown in the red curve of Figure 3b, which is dominated by Yb^{3+} ion luminescence in the NIR range centered at ~ 990 nm. A weak band-edge emission peak at ~ 400 nm was observed, which may compete with the Yb^{3+} ion luminescence for the charge recombination. The anion-exchange experiment was subsequently carried out, resulting in the production of $\text{CsPbCl}_x\text{Br}_{3-x}:\text{Yb}^{3+}$. The absorption spectrum of $\text{CsPbCl}_x\text{Br}_{3-x}:\text{Yb}^{3+}$ is displayed as the green curve in Figure 3b, with the absorption onset occurring at approximately 490 nm. The luminescence of the Yb^{3+} ion remains unchanged. The fundamental concept of QC is illustrated in the inset of Figure 3b. Here, perovskite nanocrystals can absorb high-energy photons and transfer the energy to a pair of Yb^{3+} ions, which are used for NIR luminescence. This QC process overcomes the thermalization loss for coupled Si PV in the LSC-PV system and holds huge potential for breaking the Shockley–Queisser limit.

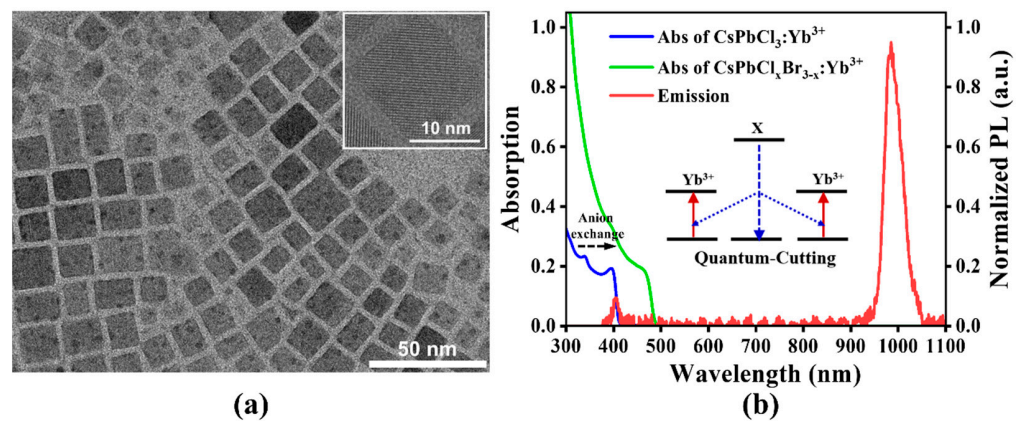


Figure 3. (a) The typical TEM image of $\text{CsPbCl}_3:\text{Yb}^{3+}$ nanocrystals; the inset is the high-resolution TEM image of a nanocrystal. (b) The absorption spectra of $\text{CsPbCl}_3:\text{Yb}^{3+}$ (blue lines) and $\text{CsPbCl}_x\text{Br}_{3-x}:\text{Yb}^{3+}$ nanocrystals (green line) in hexane. The PL spectral (red lines) of the QC emissions was excited with a 365 nm light source. The inset shows the schematic of the quantum cutting process.

To predict the performance of $\text{CsPbCl}_3:\text{Yb}^{3+}$ -based LSC and $\text{CsPbCl}_x\text{Br}_{3-x}:\text{Yb}^{3+}$ -based LSC, we simulated four nanocrystal conditions with different PLQYs using MC simulation. Figure 4a,b display the curves of η_{ext} as a function of η_{abs} (the LSC absorption efficiency for solar photons). The black dashed line represents the ideal case of a 200% PLQY of NIR emissions, while the gray dashed line shows the results for a 160% PLQY of NIR emissions. The red solid line represents the case of a 10% PLQY for band-edge emissions and a 180% PLQY for QC emissions, and the blue solid line represents the case of a 10% band-edge emissions and a 160% PLQY for QC emissions. If an additional 10% of photons are involved in the band-edge luminescence while there is a 160% PLQY of NIR emissions, leading to 20% band-edge emissions and a 160% PLQY of NIR emissions, then their η_{ext} will increase. We think most of the photons of band-edge luminescence are reabsorbed and emit light in the NIR or are lost at a sufficient concentration. If all photons are involved in the emissions and 90% of them undergo the QC progress while the remaining 10% undergo band-edge emissions, their η_{ext} will be very close to the ideal PLQY. However, there will still be a difference due to the competition between band-edge luminescence and Yb^{3+} ion luminescence. When comparing the η_{ext} of the two materials, $\text{CsPbCl}_x\text{Br}_{3-x}:\text{Yb}^{3+}$ has an η_{ext} of 12.3%, which is significantly higher than that of $\text{CsPbCl}_3:\text{Yb}^{3+}$, at 3.84%. This is due to the stronger absorption efficiency of $\text{CsPbCl}_x\text{Br}_{3-x}:\text{Yb}^{3+}$ for solar photons. The ray-tracing plots of MC simulations of the two materials are displayed in Figure 4c,d. Both materials

have dimensions of 10 cm × 10 cm, and it is visually apparent that CsPbCl_xBr_{3-x}:Yb³⁺-based LSC has a much better light concentration efficiency due to the higher η_{abs}.

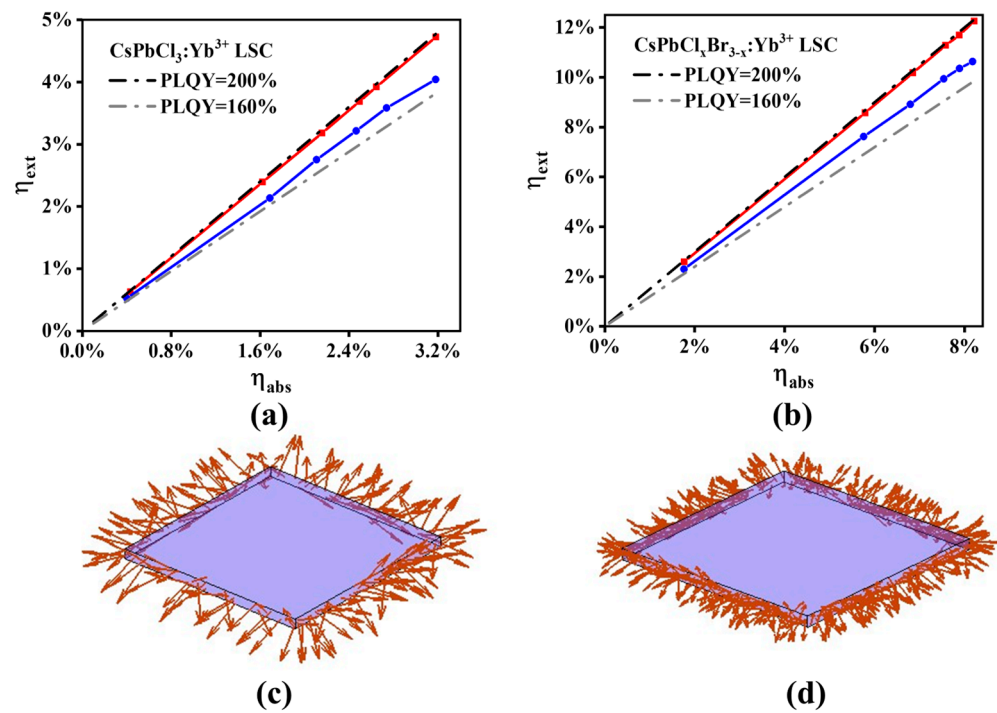


Figure 4. The external quantum efficiency η_{ext} for CsPbCl₃:Yb³⁺ (a) and CsPbCl_xBr_{3-x}:Yb³⁺ nanocrystals (b) as a function of η_{abs} from the Monte Carlo ray-tracing simulations. The black dashed lines represent the optimal PLQY of 200% and the grey dashed lines represent the PLQY of 160% without band-edge emissions. The red lines represent that 10% of the photons are involved in the band-edge emissions and 90% of the photons are involved in the Yb³⁺ emission. The blue lines represent that 10% of the photons are involved in band-edge emissions and 80% of the photons are involved in Yb³⁺ emissions. Monte Carlo ray-tracing simulation graphs for LSC devices with dimensions of 10 × 10 × 0.5 cm³ for CsPbCl₃:Yb³⁺ (c) and CsPbCl_xBr_{3-x}:Yb³⁺ nanocrystals (d). The red arrows represent the photons emitted from the edges.

MC simulations were subsequently used to investigate the effect of size on the η_{ext} of LSCs prepared by CsPbCl_xBr_{3-x}:Yb³⁺ and CsPbCl₃:Yb³⁺. The results are displayed in Figure 5a. In the ideal case, the η_{ext} of CsPbCl₃:Yb³⁺-based LSC remains at approximately 4.75% (the purple lines), while that of CsPbCl_xBr_{3-x}:Yb³⁺-based LSC remains at approximately 12.2% (the dark green lines). To account for the imperfect preparation of LSC, the scattering factor of approximately 0.012 cm⁻¹, reported by Wu et al. [17], was introduced. For CsPbCl₃:Yb³⁺-based LSC, the η_{ext} decreases from 4% to 2.2% as the size increases from 5 cm to 150 cm (the blue lines). Similarly, for CsPbCl_xBr_{3-x}:Yb³⁺-based LSC, the η_{ext} decreases from 12% to 6.3% as the size increases from 5 cm to 150 cm (the bright green lines). It is worth noting that the η_{ext} of 6.3% is still considered excellent for larger-area LSCs with a size greater than 1 m² [38,39].

The efficiency performance of systems with CsPbCl_xBr_{3-x}:Yb³⁺-based LSC and CsPbCl₃:Yb³⁺-based LSC coupled with silicon-based PV cells was predicted. The flux gains (FGs) of the two types of LSCs coupled with silicon-based PV systems at different sizes were also computationally predicted. In the LSC-PV system, the FG can represent the enhancement of the silicon-based PV photocurrent, which can be expressed as $FG = qG\eta_{ext}$. Here, q is the spectral reshaping factor, defined as the ratio between the EQE of Si PVs averaged over the LSC PL spectrum and averaged over the whole solar spectrum ($q = \langle EQE \rangle_{PL} / \langle EQE \rangle_s$). G is the geometric gain of the device, which can be expressed as $G = L/4d$, where d is the thickness of LSC, which was set as 0.5 cm in this work. Under

ideal conditions, when taking the sharp emissions of Yb^{3+} -dopants at 990 nm into account (with a shaping factor of about 1.57 for PV cells), the MC simulation results show that $\text{CsPbCl}_3:\text{Yb}^{3+}$ -based LSC can achieve an FG of 5.64 for $L = 150$ cm ($G = 75$). Similarly, $\text{CsPbCl}_x\text{Br}_{3-x}:\text{Yb}^{3+}$ -based LSC can achieve an FG of 14.51 for $L = 150$ cm ($G = 75$), indicating its potential as a solar window. The results are higher than those for all types of QD-LSC reported by Bradshaw et al. [40].

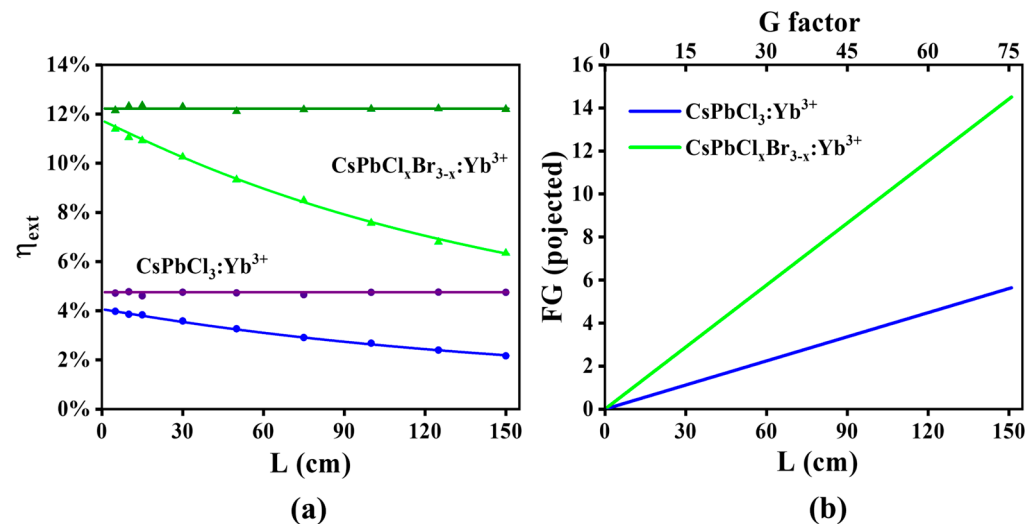


Figure 5. (a) MC simulation results of L -dependent η_{ext} for $\text{CsPbCl}_3:\text{Yb}^{3+}$ and $\text{CsPbCl}_x\text{Br}_{3-x}:\text{Yb}^{3+}$ nanocrystals. The dark green lines represent the ideal waveguide and the bright green lines represent the unideal waveguide for $\text{CsPbCl}_x\text{Br}_{3-x}:\text{Yb}^{3+}$ -based LSCs. The purple lines represent the ideal waveguide and the blue lines represent the unideal waveguide for $\text{CsPbCl}_3:\text{Yb}^{3+}$ -based LSCs. (b) MC-simulation results of flux gain (FG) for square-shaped $\text{CsPbCl}_3:\text{Yb}^{3+}$ -based LSCs (blue lines) and $\text{CsPbCl}_x\text{Br}_{3-x}:\text{Yb}^{3+}$ LSCs (green lines) with an η_{PL} of 200% and thickness of 0.5 cm.

5. Conclusions

In conclusion, we constructed an MC simulation model which is suitable to simulate the performance of the QC-LSCs. This MC simulation model can take into account the band-edge emissions and near-infrared emissions of the QC-materials. Additionally, we synthesized $\text{CsPbCl}_3:\text{Yb}^{3+}$ nanocrystals via hot injection and synthesized $\text{CsPbCl}_x\text{Br}_{3-x}:\text{Yb}^{3+}$ nanocrystal with the absorption onset of 490 nm via anion exchange. We then included the spectral data of the two materials in our MC simulation model to predict the performance of the QC-LSCs. The results demonstrate that additional band-edge emissions can lead to an improvement in the η_{ext} under the same unideal PLQY of the NIR emissions. However, if all the photons are involved in radiative recombination, the η_{ext} under the ideal PLQY will be higher due to the competition between band-edge luminescence and Yb^{3+} ion luminescence. The results also show the potential of the $\text{CsPbCl}_x\text{Br}_{3-x}:\text{Yb}^{3+}$ -based LSC, which can obtain an outstanding η_{ext} exceeding 12%. Due to the imperfections in the technique, the LSC has an indispensable scattering factor. Notably, even with such imperfections accounted for, the $\text{CsPbCl}_x\text{Br}_{3-x}:\text{Yb}^{3+}$ -based LSC can still obtain an η_{ext} exceeding 6% in the large area (>1 m²). The FG of the $\text{CsPbCl}_x\text{Br}_{3-x}:\text{Yb}^{3+}$ -based LSC-PV system can reach 14 in the large-area LSC, showing the application prospects of QC-LSC.

Author Contributions: Conceptualization, X.L. and Q.N.; methodology, X.L., Q.N. and W.L.; validation, X.L., Q.N. and W.L.; formal analysis, Q.N. and W.L.; investigation, X.L., Q.N. and W.L.; resources, X.L.; data curation, Q.N. and W.L.; writing—original draft preparation, Q.N. and W.L.; writing—review and editing, X.L., Q.N. and W.L.; visualization, X.L., Q.N. and W.L.; supervision, X.L. All authors have read and agreed to the published version of the manuscript.

Funding: This research was funded by the National Natural Science Foundation of China (No. 62274024), Natural Science Foundation Program of Sichuan Province (No. 2024NSFSC0232), Key

Teacher Start-Up Research Grant of UESTC (No. Y030202059018069) and Medical Engineering Innovations Program of UESTC.

Institutional Review Board Statement: Not applicable.

Informed Consent Statement: Not applicable.

Data Availability Statement: Data underlying the results presented in this paper are not publicly available at this time but may be obtained from the authors upon reasonable request.

Conflicts of Interest: The authors declare no conflicts of interest.

References

1. Meinardi, F.; Bruni, F.; Brovelli, S. Luminescent solar concentrators for building-integrated photovoltaics. *Nat. Rev. Mater.* **2017**, *2*, 17072. [[CrossRef](#)]
2. Biyik, E.; Araz, M.; Hepbasli, A.; Shahrestani, M.; Yao, R.; Shao, L.; Essah, E.; Oliveira, A.C.; del Caño, T.; Rico, E.; et al. A key review of building integrated photovoltaic (BIPV) systems. *Eng. Sci. Technol. Int. J.* **2017**, *20*, 833–858. [[CrossRef](#)]
3. Park, K.; Yi, J.; Yoon, S.-Y.; Park, S.M.; Kim, J.; Shin, H.-B.; Biswas, S.; Yoo, G.Y.; Moon, S.-H.; Kim, J.; et al. Luminescent solar concentrator efficiency enhanced via nearly lossless propagation pathways. *Nat. Photonics* **2024**, *18*, 177–185. [[CrossRef](#)]
4. Siripurapu, M.; Meinardi, F.; Brovelli, S.; Carulli, F. Environmental Effects on the Performance of Quantum Dot Luminescent Solar Concentrators. *ACS Photonics* **2023**, *10*, 2987–2993. [[CrossRef](#)] [[PubMed](#)]
5. Meinardi, F.; Bruni, F.; Castellan, C.; Meucci, M.; Umair, A.M.; La Rosa, M.; Catani, J.; Brovelli, S. Certification Grade Quantum Dot Luminescent Solar Concentrator Glazing with Optical Wireless Communication Capability for Connected Sustainable Architecture. *Adv. Energy Mater.* **2024**, *14*, 2304006. [[CrossRef](#)]
6. Weber, W.H.; Lambe, J. Luminescent greenhouse collector for solar radiation. *Appl. Opt.* **1976**, *15*, 2299–2300. [[CrossRef](#)]
7. Li, X.; Qi, J.; Zhu, J.; Jia, Y.; Liu, Y.; Li, Y.; Liu, H.; Li, G.; Wu, K. Low-Loss, High-Transparency Luminescent Solar Concentrators with a Bioinspired Self-Cleaning Surface. *J. Phys. Chem. Lett.* **2022**, *13*, 9177–9185. [[CrossRef](#)] [[PubMed](#)]
8. Gungor, K.; Du, J.; Klimov, V.I. General Trends in the Performance of Quantum Dot Luminescent Solar Concentrators (LSCs) Revealed Using the “Effective LSC Quality Factor”. *ACS Energy Lett.* **2022**, *7*, 1741–1749. [[CrossRef](#)]
9. Wang, L.; Chen, Y.; Lai, Y.; Zhao, X.; Zheng, K.; Wang, R.; Zhou, Y. Highly efficient and stable tandem luminescent solar concentrators based on carbon dots and CuInSe₂-xSx/ZnS quantum dots. *Nanoscale* **2024**, *16*, 188–194. [[CrossRef](#)]
10. Wang, J.; Cai, T.; Chen, O. Cesium Copper Halide Perovskite Nanocrystal-Based Photon-Managing Devices for Enhanced Ultraviolet Photon Harvesting. *Nano Lett.* **2023**, *23*, 4367–4374. [[CrossRef](#)]
11. Zhang, B.; Zhao, P.; Wilson, L.J.; Subbiah, J.; Yang, H.; Mulvaney, P.; Jones, D.J.; Ghiggino, K.P.; Wong, W.W.H. High-Performance Large-Area Luminescence Solar Concentrator Incorporating a Donor–Emitter Fluorophore System. *ACS Energy Lett.* **2019**, *4*, 1839–1844. [[CrossRef](#)]
12. Rosadoni, E.; Bellina, F.; Lessi, M.; Micheletti, C.; Ventura, F.; Pucci, A. Y-shaped alkynylimidazoles as effective push-pull fluorescent dyes for luminescent solar concentrators (LSCs). *Dye. Pigment.* **2022**, *201*, 110262. [[CrossRef](#)]
13. Lee, H.J.; Im, S.; Jung, D.; Kim, K.; Chae, J.A.; Lim, J.; Park, J.W.; Shin, D.; Char, K.; Jeong, B.G.; et al. Coherent heteroepitaxial growth of I-III-VI₂ Ag(In,Ga)S₂ colloidal nanocrystals with near-unity quantum yield for use in luminescent solar concentrators. *Nat. Commun.* **2023**, *14*, 3779. [[CrossRef](#)] [[PubMed](#)]
14. Bhosale, S.S.; Jokar, E.; Chiang, Y.-T.; Kuan, C.-H.; Khodakarami, K.; Hosseini, Z.; Chen, F.-C.; Diao, E.W.-G. Mn-Doped Organic–Inorganic Perovskite Nanocrystals for a Flexible Luminescent Solar Concentrator. *ACS Appl. Energy Mater.* **2021**, *4*, 10565–10573. [[CrossRef](#)]
15. Liu, G.; Mazzaro, R.; Wang, Y.; Zhao, H.; Vomiero, A. High efficiency sandwich structure luminescent solar concentrators based on colloidal quantum dots. *Nano Energy* **2019**, *60*, 119–126. [[CrossRef](#)]
16. Dharmo, L.; Carulli, F.; Nickl, P.; Wegner, K.D.; Hodoroaba, V.D.; Würth, C.; Brovelli, S.; Resch-Genger, U. Efficient Luminescent Solar Concentrators Based on Environmentally Friendly Cd-Free Ternary AIS/ZnS Quantum Dots. *Adv. Opt. Mater.* **2021**, *9*, 2100587. [[CrossRef](#)]
17. Wu, K.; Li, H.; Klimov, V.I. Tandem luminescent solar concentrators based on engineered quantum dots. *Nat. Photonics* **2018**, *12*, 105–110. [[CrossRef](#)]
18. Li, J.; Chen, J.; Zhao, X.; Vomiero, A.; Gong, X. High-loading of organosilane-grafted carbon dots in high-performance luminescent solar concentrators with ultrahigh transparency. *Nano Energy* **2023**, *115*, 108674. [[CrossRef](#)]
19. Wu, Y.; Zhan, Y.; Xin, W.; Cao, W.; Li, J.; Chen, M.; Jiang, X.; Wang, J.; Sun, Z. Highly Emissive Carbon Dots/Organosilicon Composites for Efficient and Stable Luminescent Solar Concentrators. *ACS Appl. Energy Mater.* **2022**, *5*, 1781–1792. [[CrossRef](#)]
20. Li, J.; Zhao, H.; Zhao, X.; Gong, X. Boosting efficiency of luminescent solar concentrators using ultra-bright carbon dots with large Stokes shift. *Nanoscale Horiz* **2022**, *8*, 83–94. [[CrossRef](#)]
21. Zhao, H.; Liu, G.; You, S.; Camargo, F.V.A.; Zavelani-Rossi, M.; Wang, X.; Sun, C.; Liu, B.; Zhang, Y.; Han, G.; et al. Gram-scale synthesis of carbon quantum dots with a large Stokes shift for the fabrication of eco-friendly and high-efficiency luminescent solar concentrators. *Energy Environ. Sci.* **2021**, *14*, 396–406. [[CrossRef](#)]

22. You, Y.; Tong, X.; Imran Channa, A.; Zhi, H.; Cai, M.; Zhao, H.; Xia, L.; Liu, G.; Zhao, H.; Wang, Z. High-efficiency luminescent solar concentrators based on Composition-tunable Eco-friendly Core/shell quantum dots. *Chem. Eng. J.* **2023**, *452*, 139490. [[CrossRef](#)]
23. Zhi, H.; Tong, X.; You, Y.; Channa, A.I.; Li, X.; Wu, J.; Selopal, G.S.; Wang, Z.M. Engineering the Optical Properties of Eco-Friendly CuGaS₂/ZnS and CuGaInS₂/ZnS Core/Shell Quantum Dots for High-Performance Tandem Luminescent Solar Concentrators. *Sol. RRL* **2023**, *7*, 2300641. [[CrossRef](#)]
24. Cai, T.; Wang, J.; Li, W.; Hills-Kimball, K.; Yang, H.; Nagaoka, Y.; Yuan, Y.; Zia, R.; Chen, O. Mn(2+)/Yb(3+) Codoped CsPbCl₃ Perovskite Nanocrystals with Triple-Wavelength Emission for Luminescent Solar Concentrators. *Adv. Sci.* **2020**, *7*, 2001317. [[CrossRef](#)] [[PubMed](#)]
25. Ding, N.; Xu, W.; Zhou, D.; Ji, Y.; Wang, Y.; Sun, R.; Bai, X.; Zhou, J.; Song, H. Extremely efficient quantum-cutting Cr³⁺, Ce³⁺, Yb³⁺ tridoped perovskite quantum dots for highly enhancing the ultraviolet response of Silicon photodetectors with external quantum efficiency exceeding 70%. *Nano Energy* **2020**, *78*, 105278. [[CrossRef](#)]
26. Zeng, M.; Artizzu, F.; Liu, J.; Singh, S.; Locardi, F.; Mara, D.; Hens, Z.; Van Deun, R. Boosting the Er³⁺ 1.5 μm Luminescence in CsPbCl₃ Perovskite Nanocrystals for Photonic Devices Operating at Telecommunication Wavelengths. *ACS Appl. Nano Mater.* **2020**, *3*, 4699–4707. [[CrossRef](#)]
27. Gao, D.; Chen, B.; Sha, X.; Zhang, Y.; Chen, X.; Wang, L.; Zhang, X.; Zhang, J.; Cao, Y.; Wang, Y.; et al. Near infrared emissions from both high efficient quantum cutting (173%) and nearly-pure-color upconversion in NaY(WO₄)₂:Er³⁺/Yb³⁺ with thermal management capability for silicon-based solar cells. *Light: Sci. Appl.* **2024**, *13*, 17. [[CrossRef](#)] [[PubMed](#)]
28. Milstein, T.J.; Kroupa, D.M.; Gamelin, D.R. Picosecond Quantum Cutting Generates Photoluminescence Quantum Yields Over 100% in Ytterbium-Doped CsPbCl₃ Nanocrystals. *Nano Lett.* **2018**, *18*, 3792–3799. [[CrossRef](#)]
29. Shen, X.; Wang, Z.; Tang, C.; Zhang, X.; Lee, B.R.; Li, X.; Li, D.; Zhang, Y.; Hu, J.; Zhao, D.; et al. Near-Infrared LEDs Based on Quantum Cutting-Activated Electroluminescence of Ytterbium Ions. *Nano Lett.* **2023**, *23*, 82–90. [[CrossRef](#)]
30. Xu, W.; Liu, J.; Dong, B.; Huang, J.; Shi, H.; Xue, X.; Liu, M. Atomic-scale imaging of ytterbium ions in lead halide perovskites. *Sci. Adv.* **2023**, *9*, eadi7931. [[CrossRef](#)]
31. Luo, X.; Ding, T.; Liu, X.; Liu, Y.; Wu, K. Quantum-Cutting Luminescent Solar Concentrators Using Ytterbium-Doped Perovskite Nanocrystals. *Nano Lett.* **2019**, *19*, 338–341. [[CrossRef](#)] [[PubMed](#)]
32. Milstein, T.J.; Kluherz, K.T.; Kroupa, D.M.; Erickson, C.S.; De Yoreo, J.J.; Gamelin, D.R. Anion Exchange and the Quantum-Cutting Energy Threshold in Ytterbium-Doped CsPb(Cl_{1-x}Br_x)₃ Perovskite Nanocrystals. *Nano Lett.* **2019**, *19*, 1931–1937. [[CrossRef](#)] [[PubMed](#)]
33. Milstein, T.J.; Roh, J.Y.D.; Jacoby, L.M.; Crane, M.J.; Sommer, D.E.; Dunham, S.T.; Gamelin, D.R. Ubiquitous Near-Band-Edge Defect State in Rare-Earth-Doped Lead-Halide Perovskites. *Chem. Mater.* **2022**, *34*, 3759–3769. [[CrossRef](#)]
34. Yoshikawa, K.; Kawasaki, H.; Yoshida, W.; Irie, T.; Konishi, K.; Nakano, K.; Uto, T.; Adachi, D.; Kanematsu, M.; Uzu, H.; et al. Silicon heterojunction solar cell with interdigitated back contacts for a photoconversion efficiency over 26%. *Nat. Energy* **2017**, *2*, 17032. [[CrossRef](#)]
35. Zhao, X.; Pan, Y.; Zuo, C.; Zhang, F.; Huang, Z.; Jiang, L.; Lai, Y.; Ding, L.; Liu, F. Ambient air-processed Cu₂ZnSn(S,Se)₄ solar cells with over 12% efficiency. *Sci. Bull.* **2021**, *66*, 880–883. [[CrossRef](#)] [[PubMed](#)]
36. He, R.; Zuo, C.; Ren, S.; Zhao, D.; Ding, L. Low-bandgap Sn–Pb perovskite solar cells. *J. Semicond.* **2021**, *42*, 060202. [[CrossRef](#)]
37. Steiner, M.A.; France, R.M.; Buencuerpo, J.; Geisz, J.F.; Nielsen, M.P.; Pusch, A.; Olavarria, W.J.; Young, M.; Ekins-Daukes, N.J. High Efficiency Inverted GaAs and GaInP/GaAs Solar Cells With Strain-Balanced GaInAs/GaAsP Quantum Wells. *Adv. Energy Mater.* **2020**, *11*, 2002874. [[CrossRef](#)]
38. Castelletto, S.; Boretti, A. Luminescence solar concentrators: A technology update. *Nano Energy* **2023**, *109*, 108269. [[CrossRef](#)]
39. Cao, M.; Zhao, X.; Gong, X. Achieving High-Efficiency Large-Area Luminescent Solar Concentrators. *JACS Au* **2023**, *3*, 25–35. [[CrossRef](#)]
40. Bradshaw, L.R.; Knowles, K.E.; McDowall, S.; Gamelin, D.R. Nanocrystals for Luminescent Solar Concentrators. *Nano Lett.* **2015**, *15*, 1315–1323. [[CrossRef](#)]

Disclaimer/Publisher’s Note: The statements, opinions and data contained in all publications are solely those of the individual author(s) and contributor(s) and not of MDPI and/or the editor(s). MDPI and/or the editor(s) disclaim responsibility for any injury to people or property resulting from any ideas, methods, instructions or products referred to in the content.